TOWARDS A HIGH FIDELITY RYDBERG INTERACTION GATE

Licenciate Thesis submitted by

Shalina Salim

Contents

1 INTRODUCTION 4

2 High fidelity trapped Rydberg ion gate 6

2.1 Trapped Rydberg ion 6

2.1.1 Paul trap 6

2.1.2 Rydberg atoms and ions 8

2.1.3 Trap effects 10

2.2 Rydberg interactions 11

2.3 Rydberg entangling gate 13

2.4 Polarization Gradient cooling 13

3 Experimental setup 17

3.1 Linear Paul Trap/Trapping ions 17

3.2 ^{88}**Sr**$^{+}$ level scheme and laser system 18

3.2.1 Loading and ionization 19

3.2.2 Cooling and Detection 20

3.2.3 Micromotion compensation 24

3.2.4 State preparation 25

3.2.5 Rydberg excitation 25

3.2.6 Measurement 27

3.2.7 Single ion addressing and UV focusing 27

3.2.8 Polarization gradient cooling 33

4 Summary and next steps 37

Abstract

Trapped Rydberg ions with their extraordinary properties serve as very good candidates for quantum computing and quantum simulation. The strong dipole-dipole interaction in Rydberg ions enables fast entangling gates between qubits. The entanglement does not involve motional quantum state to exchange information, which makes it suitable to perform gate operations in a long ion string. In this report, preliminary studies for cooling the trapped ions using polarization gradient cooling and addressing of single ion in a long ion string have been done. The results show that for cooling of multiple ions in a linear chain, a combination of Doppler cooling and polarization gradient cooling provides better cooling as compared to Doppler cooling alone. Simulations for single ion addressing shows that the focusing of the beams on the ions can be further improved by using additional optics described by the simulation. Better focusing is essential to deliver higher laser intensities to the ion such that the Rabi frequency is higher. This is important for improving the fidelity of gate operation in long ion strings.

Sammanfattning

Fångade Rydberg joner, med deras utomordentliga egenskaper, är lämpliga kandidater för kvantberäkning och kvantsimulering. Den starka dipol-dipol interaktionen mellan Rydberg joner möjliggör snabb sammanflätning mellan kvantbitar. Sådan sammanflätning utnyttjar inte jonens rörelse-kvanttillstånd för att utbyta information, vilket betyder att den kan vara lämplig för att utföra kvantoperationer i längre kedjor av joner. I denna rapport har en förundersökning för kylning av joner via ”polarisation gradient” kylning och inriktning av enskilda joner i en längre kedja utförts. Resultaten visar att flera joner i en linjär kedja kylas ner mer effektivt med en kombination av Doppler och ”polarisation gradient” kylning jämfört med endast Doppler kylning. Simuleringar för inriktningen av enskilda joner visar att laserns fokusering på jonerna kan förbättras med ytterligare optik som beskrivs i simuleringen. Förbättrad fokusering är nödvändigt så att högre laserintensitet och därefter högre Rabi frekvens uppnås på jonens position. Detta är viktigt för att öka grindoperationernas effektivitet i längre kedjor av joner.

Chapter 1

INTRODUCTION

Trapped ions have become increasingly popular for quantum computing and quantum simulation applications for almost two decades [1], [2], [3]. The high degree of state controllability and long coherence time makes them a good source for implementation of qubits- the basic element of a quantum computer, to perform quantum gates. Atomic ions can be trapped using electromagnetic fields in a linear Paul trap [4] where they can be stored for several days. Laser fields can be used to manipulate the states of the trapped ions and information is stored in qubits formed by the low lying electronic states. Gate operations can be performed on single qubit or on multiple qubits. Entanglement between multiple qubits are possible due to the interaction between the qubits by an addressing individual motional mode [5]. As the number of the qubits increases so does the complexity of the motional spectrum thus becoming complicated to address. This poses a challenge to scalability. One approach to mitigate this problem is by using a quantum charge coupled device(QCCD) architecture where an array of interconnected ion traps are used and ions are shuttled between trap regions where entanglement is possible between small number of qubits [6]. Another way to scale up trapped ion quantum computing is by using Rydberg ions, an idea proposed by Markus Müller et al. [7]. Rydberg ions are highly excited atomic ions with exaggerated properties. They have the combined advantages of exquisite control in trapped ions as well as strong dipole-dipole interaction in Rydberg atoms which makes them good candidates for quantum information processing. Strong interaction between Rydberg ions is achieved through microwave dressing, thereby enabling to perform fast and controlled motion-independent quantum gates.

This report is mainly focused on important modifications to be made in the experimental system to improve the fidelity of an entanglement gate in a long ion string. Chapter 2 mainly describes the theoretical background needed to understand the experimental system and techniques that will follow in the next chapter. In chapter 3, the experimental system is introduced with brief overview of the ion trap and the laser systems. Characterization of single ion addressing using the qubit manipulation laser as well as polarization gradient cooling in a long ion string is also discussed in this chapter. For improving the fidelity of our gate operation we should implement the radial addressing of the ions using the ultraviolet lasers. Chapter 3 also discusses, simulation of optics required for the same. The report concludes with chapter 4 where the next steps in my PhD work are outlined.

Chapter 2

High fidelity trapped Rydberg ion gate

Charged particles can be trapped and confined using electromagnetic fields. Electronic states of particles trapped in this way cooled to their lowest vibrational states, are good candidates for qubit states, which can be manipulated using resonant laser fields. In this chapter the theoretical background required to understand trapped ion Rydberg gates and interactions will be introduced.

2.1 Trapped Rydberg ion

2.1.1 Paul trap

In our system, a linear Paul trap, that uses a combination of static and time varying electric fields oscillating at radio frequencies, is used to trap and confine charged particles in three dimensions. The confining potential is applied via a set of four blade shaped electrodes together with two end cap electrodes. Figure 2.1 shows the typical configuration of the Paul trap. An RF voltage $V_0\cos\,\Omega t$ and an offset voltage V_{off} applied across the opposing pair of blade shaped electrodes creates the radial confinement in the x-y plane and a DC voltage, U_0, applied on the end cap electrodes provides the confinement along the z-direction. Together this creates an

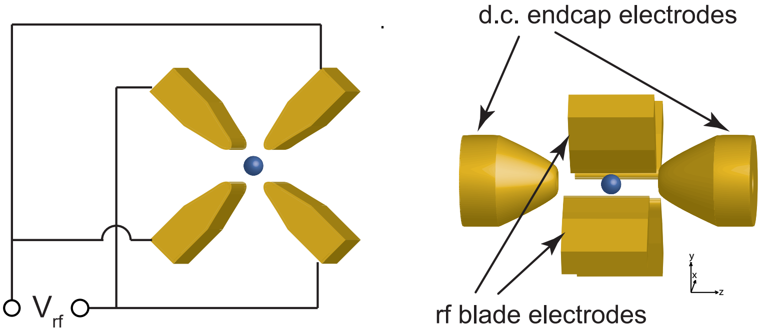

Figure 2.1: Linear Paul trap schematic diagram

oscillating quadrupole field at the centre of the trap as given by equation 2.1 [8]

$$\Phi(x,y,z,t) = \frac{x^2-y^2}{2r_0^2}(V_0\cos(\Omega t)+V_{off})+\kappa\frac{2z^2-x^2-y^2}{2z_0^2}U_0; \qquad x,y \ll r_0, z \ll z_0 \tag{2.1}$$

where r_0 is the distance from the centre of the trap to the blade shaped electrodes and z_0 is the distance from centre to the endcap electrodes. Ω is the frequency of the trap RF and κ depends on the trap geometry(κ =0.042 for our trap). Here we can define field gradients $A = \frac{V_0}{2r_0^2}$ and $B = \frac{\kappa U_0}{2z_0^2}$. The trajectory of a single charged particle in the Paul trap can be described by solutions of the Mathieu equation [4], which also gives the stability criteria for trapping [3].

The equations of motion for a single ion of mass M and charge Q in the oscillating quadrupole field in the x-direction is given as

$$m\ddot{x} = -q\nabla(x,t) = -2Qx(\frac{1}{2r_0^2}V_0\cos(\Omega t) + \frac{V_{off}}{2r_0^2} + \frac{\kappa}{2z_0^2}U_0) \tag{2.2}$$

Substituting $\alpha = \frac{V_0}{2r_0^2}$, $\gamma = \frac{V_{off}}{2r_0^2}$ and $\beta = \frac{\kappa}{2z_0^2}U_0$ and extending it to all three directions, we get

$$m\ddot{x} = -2Qx(\alpha\cos(\Omega t) + \gamma - \beta) \tag{2.3}$$

$$m\ddot{y} = 2Qy(\alpha\cos(\Omega t) + \gamma + \beta) \tag{2.4}$$

$$m\ddot{z} = -4Qz\beta \tag{2.5}$$

The above set of equations take the form of Mathieu equations as

$$\frac{dx^2}{d\tau^2} + (a_x + 2q_x\cos(2\tau) = 0 \tag{2.6}$$

$$\frac{dy^2}{d\tau^2} + (a_x + 2q_y\cos(2\tau) = 0 \tag{2.7}$$

$$\frac{dz^2}{d\tau^2} + \frac{4Q\beta z}{M} = 0 \tag{2.8}$$

where the parameters a_x, a_y and q define the regions where stable trapping is possible and are called stability parameters given as

$$a_x = \frac{8Q(\gamma - \beta)}{M\Omega^2}, \qquad a_y = \frac{8Q(\gamma + \beta)}{M\Omega^2} and \qquad q_x = q_y = q = \frac{4Q\alpha}{M\Omega^2} \tag{2.9}$$

A detailed mathematical treatment of motion of charged particle in an RF trap can be found in [3], [9]. From equation 2.9, stability parameters a and q depend on the charge(Q) to mass(m) ratio, $\frac{Q}{m}$, which could be made use to trap only the required species and expel out the unwanted isotopes or doubly ionized ions by making the trap anti-trapping for such species.

The motion of an ion is then given by the solution of the above set of differential equations and has two components: a slow secular motion in an effective harmonic trapping potential and micromotion that are fast oscillations driven by the applied trapping field. On averaging out the fast micromotion, the resulting motion of the ion is that of a harmonic oscillator and the harmonic pseudo-potential near the trap center is given by equation

$$\Psi = \frac{M}{2}(\omega_x^2 x^2 + \omega_y^2 y^2 + \omega_z^2 z^2) \tag{2.10}$$

where the secular trapping frequencies are given by

$$\omega_x = \frac{\Omega}{2}\sqrt{\frac{q^2}{2} + a_x} \qquad \omega_y = \frac{\Omega}{2}\sqrt{\frac{q^2}{2} + a_y} \qquad \omega_z = \frac{4Q\beta}{M}. \tag{2.11}$$

The radial secular frequencies are degenerate and in order to lift the degeneracy an additional DC offset voltage is applied to the blade electrodes. This enables to address each of the radial motional modes separately.

2.1.2 Rydberg atoms and ions

Rydberg atoms(ions) are highly excited atomic species with exaggerated properties which scales with the principle quantum number, n. Table 2.1 shows the dependence of relevant properties of Rydberg atoms and ions on the principle quantum number n and core charge Z .

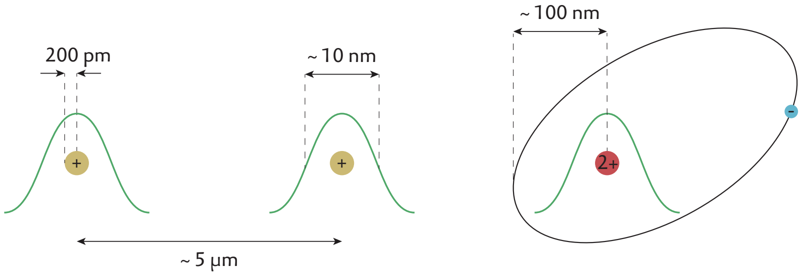

Figure 2.2: Typical length scales in our experimental system. The extend of the ion's motion(green) is larger than the extend of the electronic wavefuntion of an ion in the low lying electronic state(yellow). The classical representation of Rydberg electron orbital is shown to be ≈ 100nm which is still smaller than the typical ion separation which is ≈ 5μm.

The Rydberg electron orbital radius scales with the principal quantum number, n, as n^2 and as such the Rydberg state is much larger in magnitude in comparison to low lying states. The Rydberg electron orbital radius(≈ 100nm) in a string of such ions is small with respect to the inter-ion distance (≈5μ m). But owing to its large radius, the extend of its wavefunction exceeds that of the ion motion (≈10nm).Due to their size Rydberg states also have large polarizability and are therefore more prone to trap effects (see 2.1.3). Figure 2.2 shows the typical length scales associated with the ions in our system.

The radiative decay of a Rydberg state is strongest to low lying electronic(LLE) states. For higher Rydberg states the dipole transition moment for transition to LLE states decreases due to the decreasing overlap of the electronic wavefunctions. The natural lifetime of Rydberg sates scales as n^3 and as such Rydberg states have comparatively longer lifetimes. However at room temperature, the lifetime is limited by black body radiation and scales as n^2. Blackbody radiation can drive transitions to nearby Rydberg states with rates comparable to radiative decay to LLE states and can even cause double ionization of the Rydberg ion eventually leading to ion loss from the trap. Therefore at room temperature, in an experiment like ours, extra measures are required to reduce the temperature effects such as eliminating the use of an oven close to the trap. Trap effects also causes population loss from Rydberg states due to unwanted coupling to neighboring Rydberg states by the oscillating trapping fields and formation of Floquet states.

Property	n -scaling	Z -scaling
Binding energy E_n	n^{-2}	Z^2
Energy separation $E_n - E_{n-1}$	n^{-3}	Z^2
Orbital size r	n^2	Z^{-1}
Electric quadrupole moment $\Theta \sim r^2$	n^4	Z^{-2}
Electric polarizability α	n^7	Z^{-4}
Natural lifetime τ_{nat}	n^3	Z^{-4}
Blackbody radiation limited lifetime τ_{BBR}	n^2	Z^{-4}
Transition dipole moment of Rydberg excitation transition $\langle g\|er\|nLJ\rangle$	$n^{-3/2}$	Z^{-1}
Transition dipole moment $\langle nL'J'\|er\|nLJ\rangle$	n^2	Z^{-1}
Dipole-dipole interaction strength	n^4	Z^{-2}
Van der Waals coefficient C_6	n^{11}	Z^{-6}

Table 2.1: Property scaling of Rydberg atom(ion) with respect to the principal quantum number n and core charge Z. For Rydberg atoms $Z = +1$ and for Rydberg ions $Z = +2$. Table adapted from [10] .

2.1.3 Trap effects

Rydberg ions are highly sensitive to electric fields. There are two kind of trap effects that arise: one arising from the electric polarizability of the ion and the other due to the quadrupole coupling of states [7].

Although trapped close to the electric field minima of the trapping field, the ions with polarizability α, experience residual non-zero electric fields when moving slightly off-center. This additional fields causes an AC Stark shift ($\Delta U = -\frac{1}{2}\alpha\langle\varepsilon\rangle^2 \approx -\alpha A^2(x^2+y^2)$, where $A = \frac{V_0}{2r_0^2}$), that modifies the trapping potential, which in turn alters the trapping frequencies (figure 2.3).

The effect of this is proportional to the polarizability α and is small for LLE states while it becomes significant for Rydberg states. Following [11] the modified trapping frequencies for Rydberg state is given by equation 2.12.

$$\omega'_{x,y} \approx \sqrt{\omega_{x,y}^2 - \frac{2\alpha A^2}{M}}, \qquad \omega'_z \approx \omega_z; \tag{2.12}$$

As a result this will cause the transition frequencies between the LLE and the

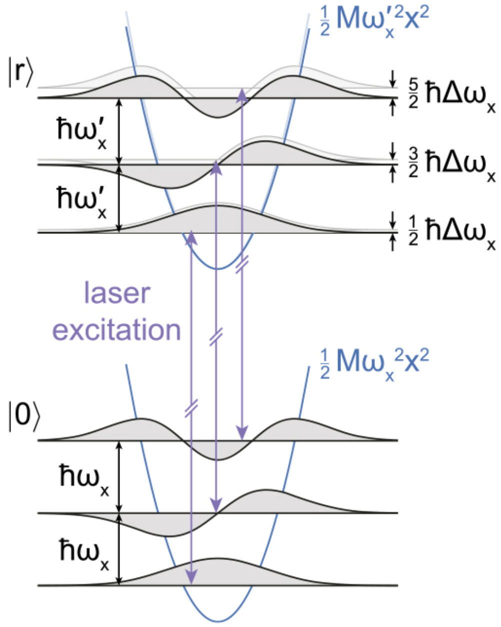

Figure 2.3: Altered trapping potential in the Rydberg ion due to its large polarizability.(Figure adapted from [10])

Rydberg state to depend on the motional phonon number. This is one cause of decoherence in the Rydberg excitation. [10], [11]

Additionally, Rydberg states with $J > \frac{1}{2}$, have very large quadrupole moments $\sim n^4$), which causes energy shifts and unwanted coupling between such states in the presence of strong quadrupole field used to trap the ion. This negatively affects the fidelity of Rydberg gates, by causing unwanted coupling to other Rydberg states during the gate sequence. The first order quadrupole effects could be mitigated by using states with $J = \frac{1}{2}$: $nS_{\frac{1}{2}}$ and $nP_{\frac{1}{2}}$, which do not have a quadrupole moment. However the effects due to second and higher order quadrupole effects still exist, and generates oscillating energy shifts due to the trapping field which gives rise to spectral sidebands. This is presented in detail in [12] .

2.2 Rydberg interactions

In trapped ions using low lying electronic states, the multi-qubit interaction is made possible through the coupling via the motional modes. However for larger system with more number of qubits, the motional mode spectrum becomes more complicated and difficult to address. This might slow down entanglement operation, lowers system performance and makes it sensitive to small changes in laser parameters, thus posing a challenge to scalability. One of the striking feature of Rydberg ions is, unlike in low lying electronic states, Rydberg ions interact via strong dipole-dipole interactions given by equation 2.13

$$\hat{V_{dd}} = \frac{1}{4\pi\epsilon_0}\frac{\hat{\mu_1}\hat{\mu_2} - 3(\hat{\mu_1}\cdot\mathbf{n})(\hat{\mu_2}\cdot\mathbf{n})}{|\mathbf{R}|^3} \tag{2.13}$$

where μ_i is the electric dipole moment, $\mathbf{R} = \mathbf{R}_2 - \mathbf{R}_1$ is the relative ion position and $\mathbf{n} = \frac{\mathbf{R}}{|\mathbf{R}|}$.

Ions in atomic eigen energy states do not have dipole moments and as such no first order effects from V_{dd}. The second order effects or the van der Waal's interaction scales with the effective core charge, Z as $\propto Z^{-6}$ (Z =2 for singly charged ion). Thus the strength of the interaction is decreased orders of magnitude in comparison to trapped atoms. However, Rydberg ions can be polarized in the presence of external field such as microwave fields. Owing to its large polarizabilities, the dipole-dipole and van der Waal's interaction strength is enhanced manifold (Table 2.1) in comparison to ground state ions. The microwave field induces a dipole moment oscillating with the microwave field perpendicular to the magnetic field vector (Figure 2.4).

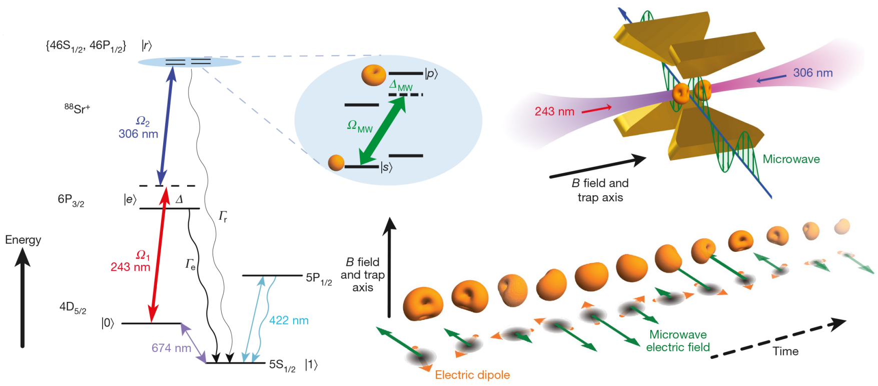

Figure 2.4: Microwave dressing of Rydberg states. The dressed Rydberg ions interact via the microwave field induced rotating dipole moment.(Figure adapted from [8])

The field couples Rydberg S and P states to create dressed states and the interaction strength can be controlled by varying the ratio of the coupling strength and detuning of the microwave field. Thus interaction between Rydberg ions via strong dipolar force allows to perform multi-qubit gate and entanglement through Rydberg interaction [13].

2.3 Rydberg entangling gate

In Rydberg ions low lying electronic states can be used as qubits and fast multi-qubit gate operations can be performed by coherently exciting to the Rydberg states and performing entanglement via dipolar interaction. Due to the interaction, the energy level of the two-ion Rydberg state is shifted out of resonance with the coupling laser field and only one of the ion can be excited to the Rydberg state. This is called Rydberg blockade. In our experiment,the interaction is not strong enough to implement an entanglement operation via Rydberg blockade , but weak enough to excite both the ions to the dressed Rydberg state. This Rydberg interaction is used to implement a phase gate as explained in detail in [13], where a two-qubit entangling gate with a fidelity of 78% has been demonstrated. One of the main sources of gate infidelity is technical errors which can be mitigated to some extend by lowering the laser linewidths and improving the laser Rabi frequencies at the ion by delivering higher laser intensities. For coherent Rydberg excitation, we use stimulated Raman adiabatic passage (STIRAP). The STIRAP transfer efficiency is dependent on the laser Rabi frequencies which are proportional to the laser intensities. If the intensity is not sufficient this leads to non-adiabaticity and eventually population loss from the intermediate state. The laser intensity on the ion can be improved by improving the laser focusing on the ions. In the present setup the Rydberg lasers are delivered in the axial direction where the confinement is weak and thus larger spread of the motional wavefuntion. This causes dephasing due to random phase introduced during the Rydberg excitation. So in our experiment errors arising from this can be reduced by using radial addressing, since the confinement is stronger in this direction and therefore smaller spread of the motional wavefunction and lower temperature. The laser focusing and radial addressing are discussed in section 3.2.7. For larger ion crystal, since the axial confinement is weak, ground state cooling can be improved by implementing polarization gradient cooling (section 2.4).

2.4 Polarization Gradient cooling

For performing high fidelity quantum computation and simulation it is essential to be able to prepare string of ions in the motional ground state with efficient cooling of the motional modes. Apart from achieving ground state cooling there are other factors which needs to be addressed such as speed of cooling and range of motional frequencies that can be cooled. Although conventional methods such as resolved sideband cooling and Raman techniques are well suited for this application, they are limited when it comes to low frequency motional modes. Large Coulomb crystal or string of ions have low axial frequencies and gives rise to collective motional modes. Polarization gradient cooling, a Sisyphus cooling technique, has been used to cool neutral atoms [14] to sub-Doppler temperature and can be used to cool collective vibrational modes in a long ion string to low vibrational quantum numbers ([15], [16]) and hence improving gate fidelity.

Following the theory from [15] and [16], we consider an ion of mass m trapped in a harmonic potential $U_{trap} = \frac{1}{2}m\omega_z^2 z^2$ with trapping frequency ω_z. A transition between angular momentum quantum numbers $j_g = 1/2$ and $j_e = 1/2$ is excited off-resonantly by a pair of counter-propagating orthogonally polarized laser beams produces a standing wave pattern with polarization gradient along the direction of the laser propagation (creating the so called $lin- \perp -lin$ configuration). Assuming that the laser beams propagate along the quantization axis z, the ions will interact only with the $\sigma_\pm$ photons. This varying polarization, produces ac Stark shift on the Zeeman sub-levels, $|+\rangle$ and $|-\rangle$, of the ground state which depends on the phase difference ϕ between the counter-propagating beams. As a result the ion experiences an effective harmonic potential which is oscillatory in nature given by equation 2.14. [15]

$$U_\pm = U_{trap} + \frac{1}{3}\Delta s \mp \frac{1}{3}\Delta s\ sin(2kz + 2\phi) \tag{2.14}$$

where Δ is the detuning of the laser field from the dipole transition and ϕ determines the position of the polarization gradient with respect to the trap center. The saturation parameter s gives the intensity of the cooling beams and is given by equation 2.15, where Γ is the linewidth and Ω is the Rabi frequency of the transition.

$$s = \frac{\Omega^2/2}{\Gamma^2/4 + \Delta^2} \tag{2.15}$$

For weak excitation, $s \ll 1$, the excited state can be adiabatically eliminated and population is exchanged between the Zeeman sub-levels of the ground state via off-resonant Raman transitions. The spatially varying polarization also creates a periodic variation in the transition rates(equation 2.16) between the Zeeman sublevels [16].

$$\Gamma_{\pm\to\mp} = \frac{1}{9}\Gamma s(1 \mp sin(2\phi)) \tag{2.16}$$

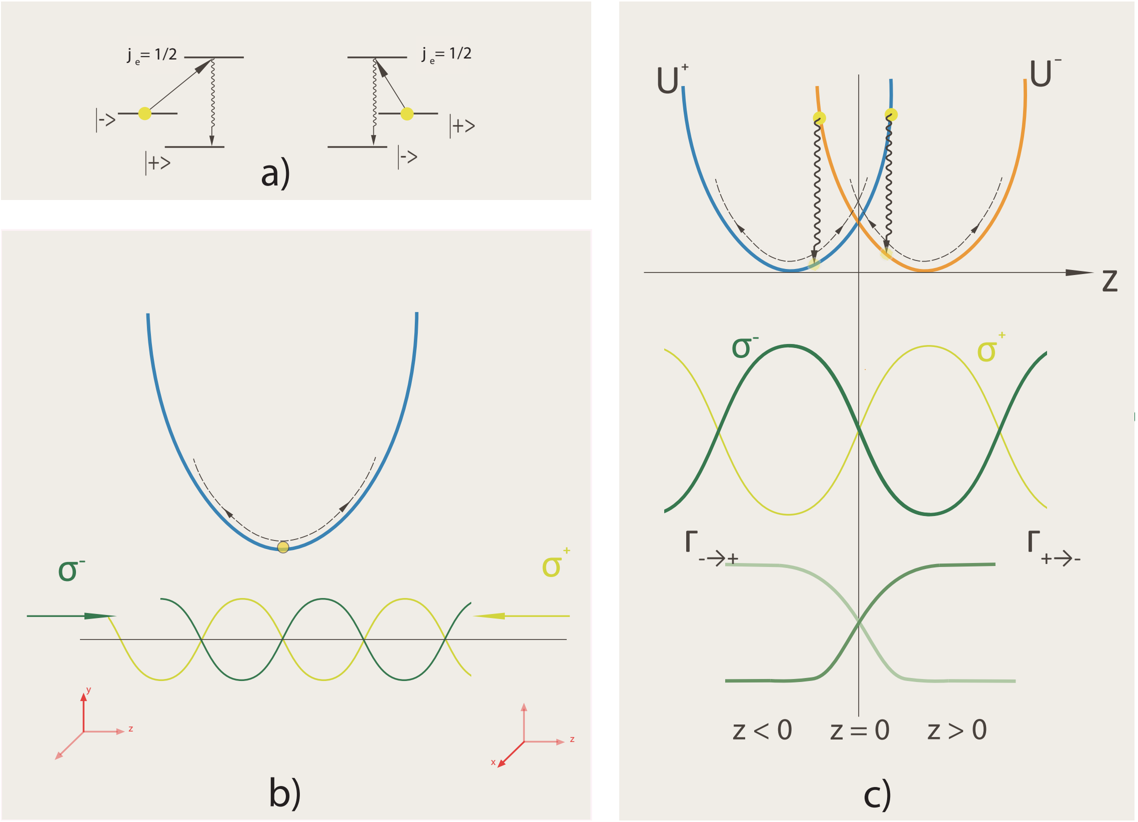

Figure 2.5: Sisyphus cooling mechanism. a) Shows the off resonant Raman transitions between Zeeman sublevels $|\pm\rangle = | j_g, m = \pm\frac{1}{2}\rangle$. b) The ion in a harmonic potential subjected to counter-propogating laser beam of orthogonal linear polarization creating a gradient of polarization along the direction of ion motion. c) The effective potential $U_\pm$ on the two Zeeman sublevels $|\pm\rangle$. Whenever the ion moves from $z = 0$ and climbs up the potential, it becomes resonant with the $\sigma^\pm$ light which transfers the population to $U_\mp$ with transition rates $\Gamma_{\pm\to\mp}$.

The polarization gradient cooling mechanism can be understood from the figure 2.5. For ion position $z < 0$ (figure 2.5c), where the light has a polarization σ^+, the transition from $|-\rangle$ to $j_e = 1/2$ (figure 2.5a) is favored such that the ion undergoes a Raman transition from $|-\rangle$ to $|+\rangle$, and the ion is transferred from the top of hill in the potential U_- of state $|-\rangle$, to valley in the potential U_+ of state $|+\rangle$. The ion remains in this potential until it reached the position $z > 0$, where the σ^- polarization aids the optical pumping back to $|-\rangle$. The ion loses its kinetic energy during each transfer and this continues until the ion no longer can climb up the hill and is stuck at the lowest point in the valley[17]. Here we assume that the pumping rate is slow with respect to the ion's oscillation in the harmonic trap. An equilibrium temperature is reached when a balance is reached between cooling and the spontaneous decay and the ion is thus cooled down. Thorough calculation shows that motional state population of $< n >\approx 1$ can be reached with cooling rates on the order of 10000 quanta/s for typical trapping parameters ([15], [16]). This could be extended to a string of ions, where each ion experiences the polarization gradient at its position. A detailed description of the cooling rates and limit can be found in [15, 16]. Details of experimental implementation are described in section 3.2.8.

Chapter 3

Experimental setup

In this chapter I briefly explain the experimental system, Rydberg excitation, polarization gradient cooling and single ion addressing. The experiment consist of a linear Paul trap in an ultra-high vacuum ($\sim 10^{-10}$mbar) chamber, where Strontium ions, $^{88}\mathrm{Sr}^{+}$, are confined. Strontium is an alkaline earth metal and has a simple outer shell configuration. Singly charged strontium ion has a single valence electron and the inner electrons are closely bound to the core which makes it possible to approximate it to a two-body system. The lasers required to excite the relevant transitions are readily available from diode laser based systems [18]. Furthermore the Rydberg excitation can be done through a two-photon excitation and the laser frequencies required for this lies in the vacuum ultraviolet(VUV) region making the experimental system simpler. Detailed explanation of the system can be found in [19, 10].

3.1 Linear Paul Trap/Trapping ions

As described in section 2.1.1, the linear Paul trap uses a combination of static and oscillating electric fields to trap the ion in three dimensions. The design of our ion trap is adapted from the Innsbruck trap design [19] and consists of gold plated blade like electrodes and dc end cap electrodes with drilled hole for optical access along the axial direction. The RF electrodes are separated by a distance of 0.7mm and the end cap electrodes by 5mm. The trap assembly consisting of the blade electrodes, the dc electrodes and the mount are made of titanium and the spacer holding the electrodes from sapphire. The entire trap assembly is mounted inside a ultra high vacuum chamber with a spherical octagon configuration. Further details of the vacuum chamber, fabrication and assembly are described in [19].

In our experiment the oscillating quadrupole field is driven at $\Omega_{rf} = 18.2$MHz and the typical trapping frequencies in the radial direction (x and y) are $\omega_{x,y} \approx 2\pi \times 1.7$MHz and in the axial direction is $\omega_z \approx 2\pi \times 840$kHz [10] corresponding to a field gradient of $A \approx 8.4 \times 10^8$ Vm^{-2}. The static field has a gradient of $B \approx 6.8 \times 10^6$ Vm^{-2}. The radial trapping frequencies are separated by around 70kHz by applying a small DC voltage on the trap electrodes. Figure 3.1 shows the experimental set up with all the optical access for different laser beams.

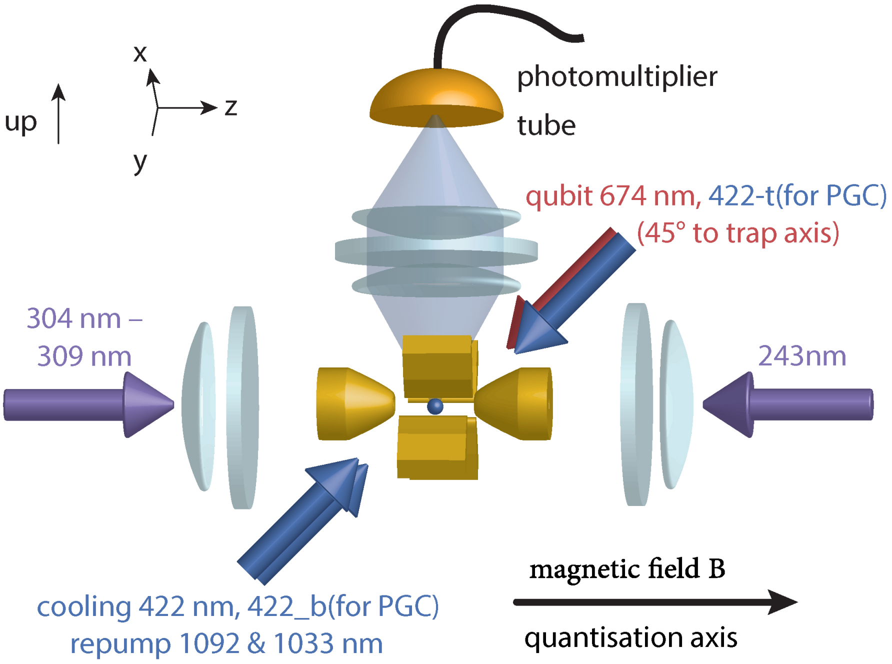

Figure 3.1: Ion trap setup schematic diagram with optical access (side view). The quantization axis is defined by the magnetic field direction which is parallel to the axis of the trap. Here 422-t and 422-b stands for the polarization gradient cooling beams from the top and bottom respectively.

3.2 ^{88}Sr$^+$ level scheme and laser system

^{88}Sr is the most common isotope of strontium with natural abundance of 83%. Figure 3.2 shows the energy levels and relevant transitions of ^{88}Sr$^+$ ions.

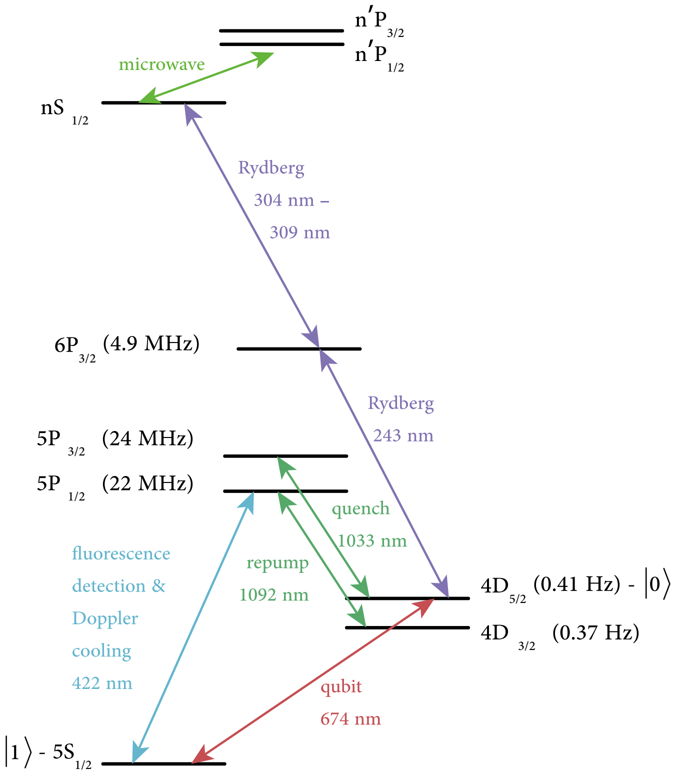

Figure 3.2: Level scheme for $^{88}Sr^{+}$. (Figure adapted from [8])

3.2.1 Loading and ionization

There are three commonly used methods of loading ions: electron impact ionization of neutral atom beam, photoionization of neutral atom beam and laser ablation of solid target followed by ionization of the neutral atoms. Our system uses the latter method. Our ablation loading uses a 515nm solid-state laser which generates ≈ 1ns laser pulse with a repetition rate of 2kHz. Ablation loading is a fast loading technique and also eliminates the need for a neutral gas beam, generated by heating up an oven. Thus blackbody radiation associated with having the oven can be avoided. The technique is explained in more detail in [20]. After ablation loading, photoionization is used to ionize the neutral atoms at the centre of the trap, via two photon excitation using two lasers at 405nm and 461nm which are overlapped, fiber coupled and sent to the trap through a single mode photonic crystal fiber. The 461nm laser excites the atom into a P state via the dipole transition $5s^2\ {}^1\mathrm{S}_0 \rightarrow 5s5p\ {}^1\mathrm{P}_1$, from where the 405nm laser excites it to an autoionization state above the ionization limit (Figure 3.3).[18]

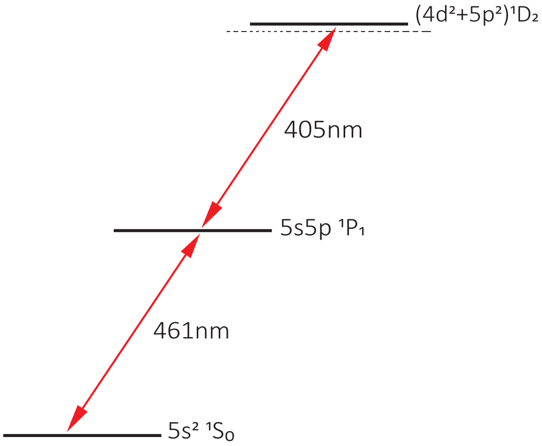

Figure 3.3: Level scheme for photoionization. The 461nm laser excites the atom into a P state via the dipole transition $5s^2\ {}^1\mathrm{S}_0 \rightarrow 5s5p\ {}^1\mathrm{P}_1$, from where the 405nm laser excites it to an autoionization state $(4d^2 + 5p^2)\ {}^1\mathrm{D}_2$, above the ionization limit.[18]

3.2.2 Cooling and Detection

Before each experiment the ion is cooled and prepared in the motional ground state. For this, first Doppler cooling (details in [10]) is used to cool the ion to the Lamb-Dicke regime and then resolved sideband cooling is used to cool the ion below the Doppler limit close to the motional ground state. In theory, a set of counter propagating laser beams detuned from resonance acts on the moving ions, and due to the Doppler effect causes absorption of the photons opposite to the direction of the ion's velocity followed by spontaneous emission in random direction. This leads to a force on the ions which dampens its motion and when applied from all three directions leads to slowing down of the ion [17]. In our experiment we use laser beam at 422nm, red detuned from the cycling transition $5S_{1/2} \leftrightarrow 5P_{1/2}$, for Doppler cooling. It is sent to the trap at an angle such that it has k-vector along all three trap axes, thus cooling the ion in all directions. After Doppler cooling, the mean phonon number in axial mode is $\bar{n_z} \approx 16$ and in the radial modes are $\bar{n_x}, \bar{n_y} \approx 12$, when typical trapping frequencies are used[10]. There is 6% probability that the ions can also decay to the metastable state $4D_{3/2}$ from the $5P_{1/2}$ state. It is important to re-pump population back to $5S_{1/2}$. We use a laser beam at 1092nm to avoid optical pumping to $4D_{3/2}$ via $5P_{1/2}$ (Figure 3.4). The 422nm light scattered by the ions is used for fluorescence detection on a photomultiplier tube (PMT) and on an electron multiplying charge coupled device(EMCCD) camera.

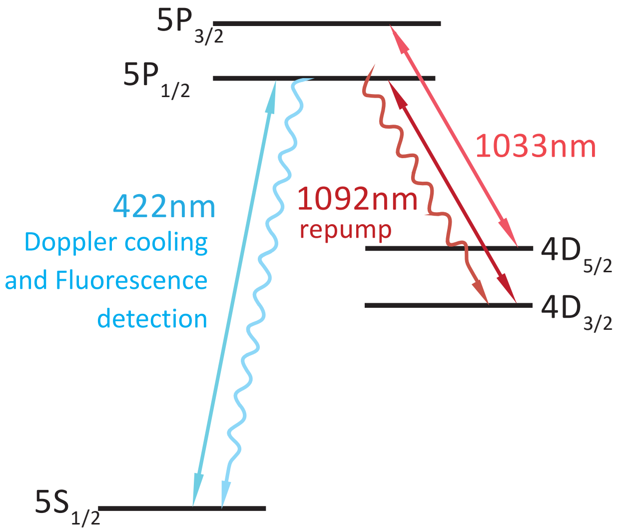

Figure 3.4: Level scheme for Doppler cooling and fluorescence detection. The 422nm laser is used for Doppler cooling along with the 1092nm repumping laser to prevent loss of population to the $4D_{3/2}$ level

.

Additionally for state initialization using optical pumping and resolved side band cooling, a laser beam at 1033nm is used, which pumps out any population that was initially in metastable state $4D_{5/2}$.

Resolved sideband cooling

Ground state cooling beyond the Doppler limit is done using resolved sideband cooling mechanism. The motion of an ion with trapping frequency ω can be treated as a harmonic oscillator. While interacting with a resonant laser at frequency ν, its spectrum consists of a carrier at frequency ν and symmetrically spaced sidebands at frequencies $\omega_L = \nu \pm \omega$ (the sideband at frequency $\nu + \omega$ is called the blue sideband and the sideband at frequency $\nu - \omega$ is called the red sideband) as shown in figure 3.5. Driving a red sideband decreases the motional phonon number, while driving blue sideband increases it. The strength with which the phonon number changing transitions are driven depends on the Lamb- Dicke parameter, η, which is given by

$$\eta = kcos\phi\sqrt{\frac{\hbar}{2M\omega}} \tag{3.1}$$

where k is the laser wave vector,ϕ is the angle between the laser light and mode axis, M is the mass of the ion and ω is the frequency of the motional mode. In the

Lamb-Dicke regime, defined by the inequality $\eta^2(2n+1) << 1$, the relative strength with which the carrier and first-order sidebands are driven are given by the following equations [21]

$$\Omega_{n\to n} = (1-\eta^2 n)\Omega_0 \tag{3.2}$$

$$\Omega_{n\to n+1} = \eta\sqrt{n+1}\Omega_0 \tag{3.3}$$

$$\Omega_{n\to n-1} = \eta\sqrt{n}\Omega_0 \tag{3.4}$$

Following figure 3.5, for an ion in the motional state n (where n is the phonon number state), driving a red sideband would take it to the excited state with a motional state n-1. Within the Lamb-Dicke regime, the natural decay would then de-excite it to the ground state without affecting the motional state, thus returning the ion to n-1 motional state. Thus the ion is now in a lower motional state compared to what it started with. On further driving red sidebands, the process of absorption and spontaneous emission continues until the ion reaches the motional ground state where it cannot be excited by a red sideband transition anymore.

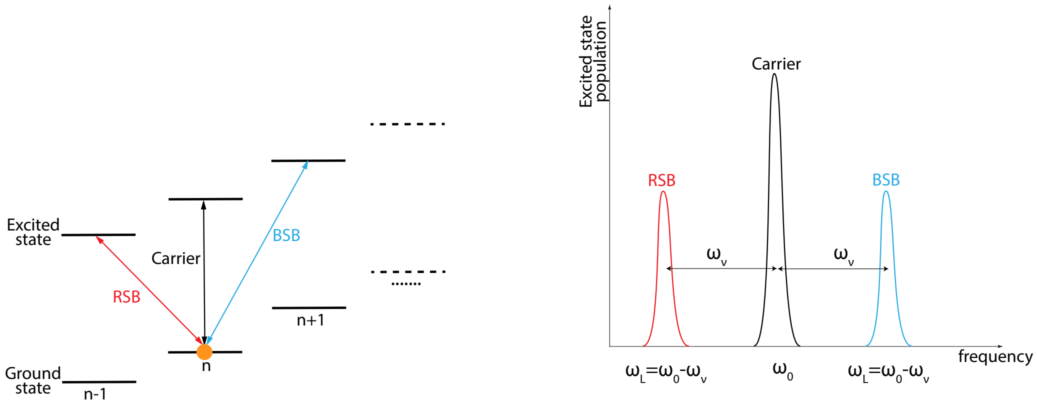

Figure 3.5: Pictorial representation of carrier and sideband transitions.

In our experiment we drive red sideband on the $5S_{\frac{1}{2}} \leftrightarrow 4D_{\frac{5}{2}}$ transition at 674nm. This excitation to $4D_{\frac{5}{2}}$ reduces the phonon number by 1, and the population can either decay back to $5S_{\frac{1}{2}}$ retaining the phonon number by loosing another phonon or by regaining the lost phonon. Since we operate in the Lamb-Dicke regime, the decay process retaining the phonon is favoured. Hence, on an average this process leads to a reduction in the phonon number and is continued until the red sideband can no longer be driven. The process is sped by reducing the effective lifetime of the $4D_{\frac{5}{2}}$ metastable state by coupling the $4D_{\frac{5}{2}}$ state to $5P_{\frac{3}{2}}$ using 1033nm laser (figure 3.6).

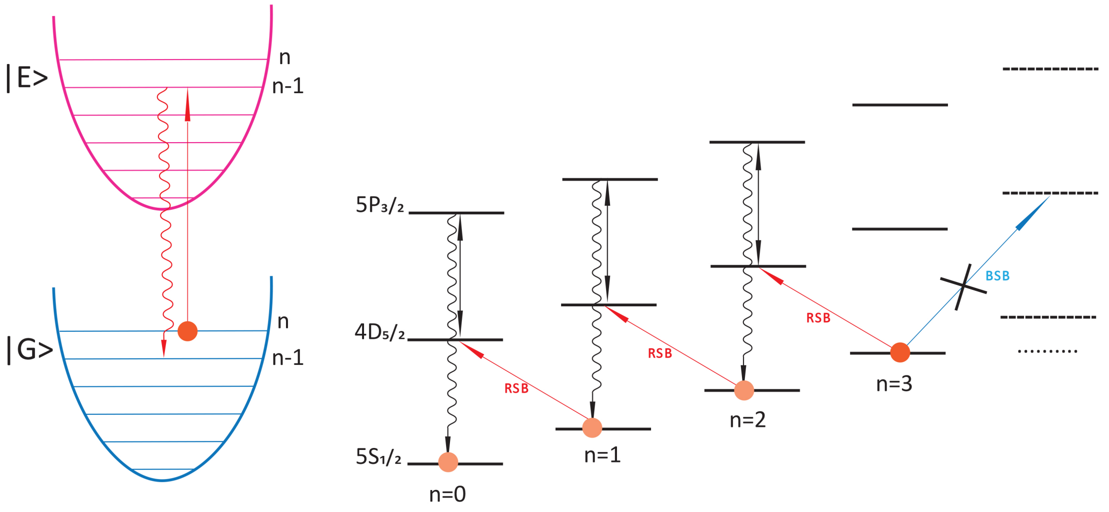

Figure 3.6: Resolved sideband cooling by driving first order red sidebands on the qubit transition.

.

To address and cool the radial and axial motional modes, the 674nm beam is sent from the radial and angled directions with respect to the trap axis. The quality of cooling is characterized by measuring the mean vibrational quantum number which is a measure of the ion temperature. In the Lamb-Dicke regime, any of the following methods can be used to measure the mean phonon number after cooling [21]

i) comparing the excited state population when incoherently exciting a red sideband vs a blue sideband: Exciting a blue sideband leads to half of the population in the ground state being transferred to the excited state whereas exciting a red sideband leads to half of the population not in the ground state being excited to the excited state. Thus the absorption strength on the red and the blue sideband gives the ground state population p_0 as

$$p_0 = 1 - \frac{p(\Delta = -\omega)}{p(\Delta = +\omega)} \tag{3.5}$$

ii) comparing the absorption strength for the carrier and the red sideband: The mean phonon number can be determined from the ratio of the absorption probabilities on first order red sideband and that of the carrier, when excited incoherently without saturating the carrier as given by the equation

$$\frac{p(\Delta = -\omega)}{p(\Delta = 0)} = \eta^2 \bar{n} \tag{3.6}$$

where η is the Lamb-Dicke parameter and $\bar{n}$ is the mean phonon number.
iii) Coherent excitation of the carrier: The Rabi frequency of the carrier depends on the motional state. Following the calculation from [21] the population in the excited state is approximated to

$$p_t = \frac{1}{2}\{1 - \frac{\cos(2\Omega t) + 2\Omega t \eta^2(\bar{n}+1)\sin(2\Omega t)}{1 + (2\Omega t \eta^2(\bar{n}+1))^2}\} \tag{3.7}$$

where t is the pulse length and Ω is the Rabi frequency of the carrier. In our experiment after Doppler cooling the ion to the Lamb-Dicke regime, to bring it close to the motional ground state, sideband cooling is used to further bring down the temperature. The cooling beams are switched off for a certain wait time to allow the ion to heat up. A laser pulse, which is tuned either to the red or the blue sideband of the qubit transition, is then used to drive sideband Rabi oscillations.

To determine the mean phonon number we use the first method described above. Following the calculation from [22], the ratio R of the excitation probability on the red and the blue sideband is related to the mean phonon number $\bar{n}$ as,

$$R = \frac{p(\Delta = -\omega)}{p(\Delta = +\omega)} = \frac{\bar{n}}{\bar{n}+1} \tag{3.8}$$

Measuring R for different delays allows to determine the heating rate. Details of this method is found in [22]. When using typical trapping frequencies, after resolved sideband cooling the mean phonon numbers are $\bar{n}_x, \bar{n}_y, \bar{n}_z \approx 0.2$. Below this limit the temperature measurements become difficult due to the off-resonant transitions driven by the servo bumps of our qubit transition laser.

3.2.3 Micromotion compensation

Various factors such as stray fields and imperfections in the trap geometry contribute to non-overlapping of the static and oscillating trapping fields and causes excess micromotion. This excess micromotion gives rise to excess heating and modification to transition lineshapes and shift in resonance frequencies which are unwanted. Rydberg ions have very large polarizabilities and additional electric fields caused by the excess micromotion induces Stark shift which alters the lineshape of the Rydberg resonance [12]. Therefore excess micromotion has to be minimized if not eliminated. In our experiment we use additional electrodes to compensate for excess micromotion. The voltages applied to these electrodes push the ion to the position where the null of the static and the oscillating quadrupole fields overlap. In the experiment, we first determine the micromotion sideband resonance line by doing a frequency scan of a quadrupole qubit transition detuned by the RF frequency $\Omega = 18$MHz. Then a scan of the compensation electrode voltage is performed and the strength of the micromotion sideband is observed. The voltage at which the strength of the micromotion sideband is minimum gives the voltage where the nulls of the static and oscillating field overlap and micromotion is compensated. This is done iteratively in two directions in order to compensate for the excess micromotion in two radial directions. The various methods to compensate for excess micromotion are detailed in [23, 24, 25].

3.2.4 State preparation

The initial state of the ion is prepared either in state $\mid 1\rangle$ corresponding to a Zeeman sublevel $5S_{\frac{1}{2}}$, $m_j = -\frac{1}{2}$ by optical pumping or in state $\mid 0\rangle$ corresponding to $4D_{\frac{5}{2}}$, $m_j = -\frac{5}{2}$ using frequency resolved optical pumping and a π pulse on the 674nm $\mid 1\rangle \leftrightarrow\mid 0\rangle$ transition . The ion can also be prepared in a superposition of states $\mid 0\rangle$ and $\mid 1\rangle$ using optical pumping and then driving a $\frac{\pi}{2}$ pulse on the 674nm $\mid 1\rangle \leftrightarrow\mid 0\rangle$ transition with a phase ϕ. More details are found in [10].

3.2.5 Rydberg excitation

In our experiment, excitation to Rydberg state is done using two- photon excitation [10] using two counterpropagating ultraviolet lasers at 243nm and 304-309nm. An ion prepared in the state $\mid 0\rangle$ - $4D_{\frac{5}{2}}$ is exited to an intermediate state $\mid e\rangle$ - $6P_{\frac{3}{2}}$ in the first excitation step using 243nm laser and the 304-309nm laser excites the ion from the intermediate state to the Rydberg state $\mid r\rangle$ (Figure 3.7). Coherent excitation to Rydberg states via two-photon excitation is done using STIRAP(Stimulated Raman adiabatic passage). STIRAP is a method to transfer population between two states by coupling to an intermediate state, without populating the intermediate state.

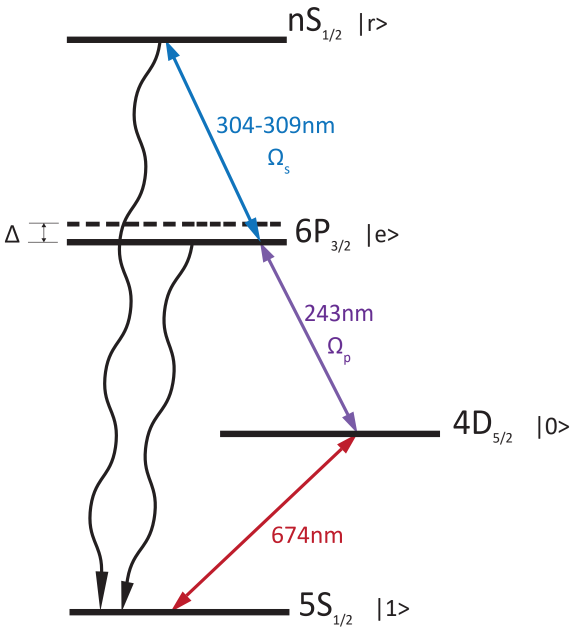

Figure 3.7: Level scheme for Rydberg excitation.

.

This is implemented using a pulse sequence where Ω_p and Ω_s are varied sinusoidally during the rise time t_{rise} as

$$\Omega_p(t) = \Omega_{peak} \sin \frac{\pi t}{2t_{rise}} \qquad \Omega_s(t) = \Omega_{peak} \cos \frac{\pi t}{2t_{rise}} \tag{3.9}$$

where Ω_{peak} is the peak Rabi frequency which is same for both Ω_s and Ω_p. Following [26], the adiabaticity condition is given as

$$\frac{\pi}{2t_{rise}} \ll \Omega_{peak} \tag{3.10}$$

In our experiment Ω_{peak} is limited by Ω_p due to the lesser availability of the 243nm laser intensity at the ion. So, to satisfy the adiabaticity criterion, t_{rise} is made longer. However if t_{rise} is too long, it leads to losses due to Rydberg state decay and decoherence due to finite laser linewidth. The STIRAP transfer efficiency can be improved by using higher laser light intensities or by using higher Rydberg state with longer lifetimes. By implementing better focussing of the UV light on the ion, Rabi frequency can be improved as explained in 3.2.7.

3.2.6 Measurement

Electron shelving is used to distinguish between states $| \, 0\rangle$ and $| \, 1\rangle$. When the ion is in state $| \, 1\rangle$, it scatters a lot of the 422nm light through the fast cycling transition which is captured as PMT counts. Whereas, when it is in state $| \, 0\rangle$ it scatters almost no 422nm light giving low count rates on the PMT corresponding to the background noise. $| \, 1\rangle$ is called the bright state and $| \, 0\rangle$ is called the dark state.

3.2.7 Single ion addressing and UV focusing

To implement quantum gates in a long ion string, single ion addressing is necessary to be able to control and realize addressed manipulation of each ion individually with 674nm for arbitrary single qubit rotations. In doing so, the internal state of the neighboring ions should remain unchanged. Experimentally this is done by tightly focusing the addressing beam on the ion by taking advantage of the optics already set up for fluorescence imaging, and measuring the Rabi frequency.

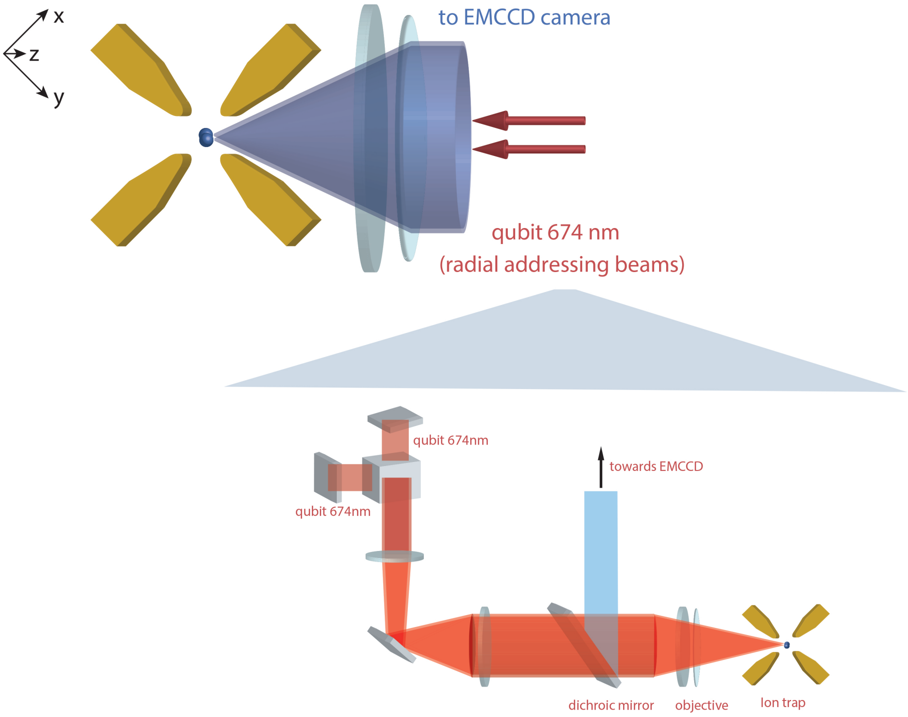

Figure 3.8: Single ion addressing optics set up. In this setup two individual laser beams are overlapped on a beam splitter and directed onto different ions in an ion string

Figure, 3.8 shows the optics set up for delivering the addressing 674nm beams on the ions. Details of the optics design can be found in [20].
For the purpose of characterizing the single ion addressing, two ions were loaded and at axial trapping frequency of ω_z= 1.27MHz, the distance between the centre of the ions were calculated to be roughly 3.5μm. The position of the ions were marked using the EMCCD camera software. Using the DC end cap electrodes a single ion was then moved to one of the two marked positions. Two addressing 674nm beams were set up in the radial direction and at each of the two positions, the Rabi frequency was measured by driving resonant carrier transition using a pi-pulse. How effectively the ion can be addressed at a particular position, depends on the ratio of the Rabi frequencies of the two beams at that position. Figure 3.9 shows Rabi oscillations on the two ions while using only one of two addressing beams. The effect of addressing can be clearly seen from the figure that the addressing beam drives Rabi oscillation on the addressed ion much better than the neighboring ion. From figure 3.9a, the Rabi frequency of the left ion, which is addressed by the laser beam coming from the left, is around 9.5times faster compared to the right ion that is not addressed. Similarly from figure 3.9b, the Rabi frequency of the right ion, which is addressed by the laser beam coming from the right, is around 7.5times

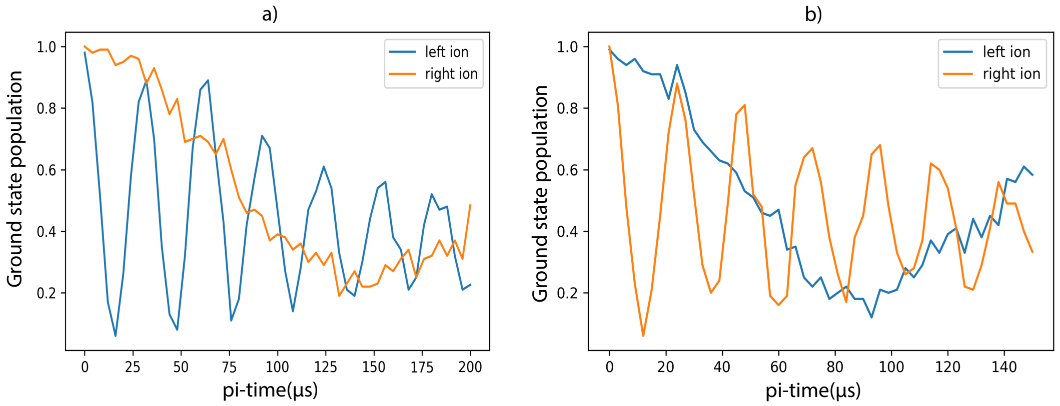

Figure 3.9: a) Rabi oscillation on the ions using addressing beam on the left side ion's position. b) Rabi oscillation on the ions using addressing beam on the right side ion's position.

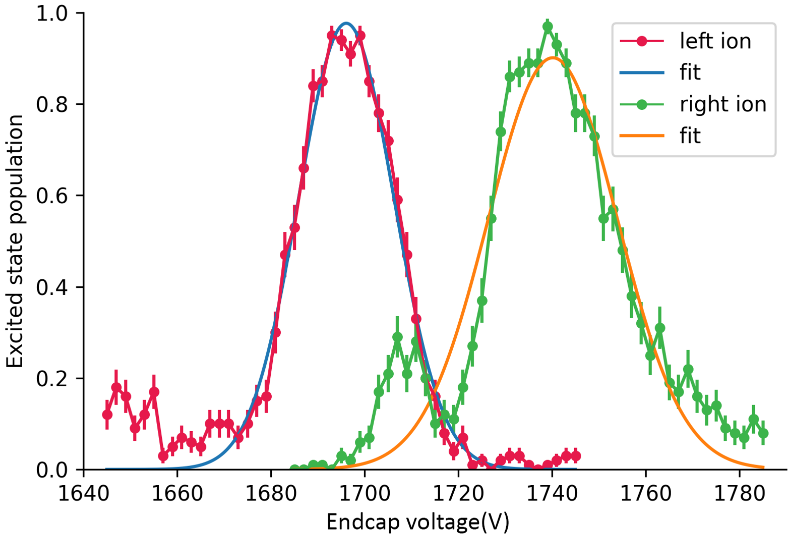

Figure 3.10: Scan of the electrode voltage to find the beam waist of the laser beam at the ion position.

faster compared to the left ion that is not addressed. The difference in the strength of Rabi oscillations on the two ions is due to the fact that the two laser beams are not equally focused on the ions. This can further be improved by improving the focusing of the addressing beam on the ion. This set up will be later replaced by implementing an acousto-optic deflector(AOD) for individual ion addressing.

The beam waist at the ion was also characterized by then scanning the endcap electrode voltage so as to move the ion through the laser beam (Figure 3.10). From the scan the full width half maximum(FWHM) of the two addressing beams were obtained after fitting the data with a Gaussian. From this, for a distance of 3.5μm between the ions, the beam waist at the ion position was calculated to be around 1.9μm and 2.5μm for the beams addressing the left and the right side ions respectively.

Zemax OpticStudio simulation for addressing with the objective for 674nm gives a diffraction limited spot radius of 2.085μm [20] which corresponds to a FWHM of 0.88μm. Therefore the present addressing set up needs further optimization to improve the focusing on multiple ions. The efficiency of coherent control and performing quantum gates depends on the coupling of the laser beams with the states. Focusing of the UV beam increases the intensity delivered at the ion's position thereby improving the Rabi frequency of the Rydberg transition and hence increase the fidelity with which entanglement gates could be performed. Implementing the focusing optics from the radial direction, where the confinement is stronger, would reduce the effect of temperature and motion of the ion. For this new optics has to be set up to deliver the UV beams from the radial direction. The preliminary design of the optics has been done in Zemax OpticStudio. From the simulation a diffraction limited airy radius of $\approx 0.8\ \mu m$ for 305nm laser (figure 3.11b) and $\approx 0.7\ \mu m$ for 243nm beam(figure 3.12b). The next steps would be to set up the UV optics in a counter-propogating manner in the radial direction.The 305nm optics will be delivered to the ion from the same direction as the addressing 674nm beam, whereas the 243nm beam will be sent from the opposite direction. For simultaneous arbitrary single qubit rotations on different ions in a string of ions, AOD will be incorporated in the set up to address multiple ions at the same time by driving the AOD with multi-chromatic frequencies.

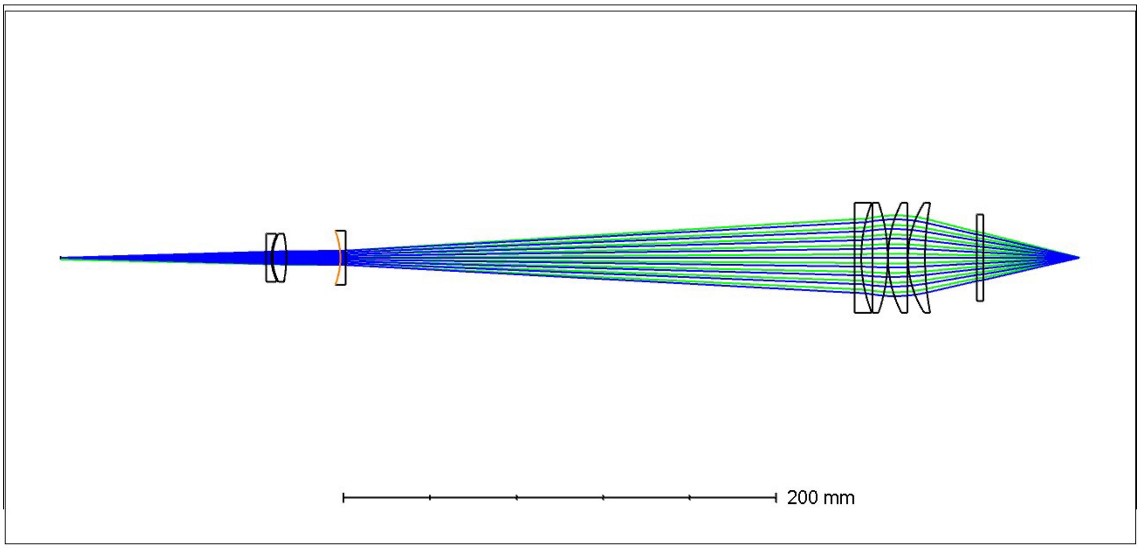

(a) Zemax OpticStudio design layout for the 305nm laser focussing.

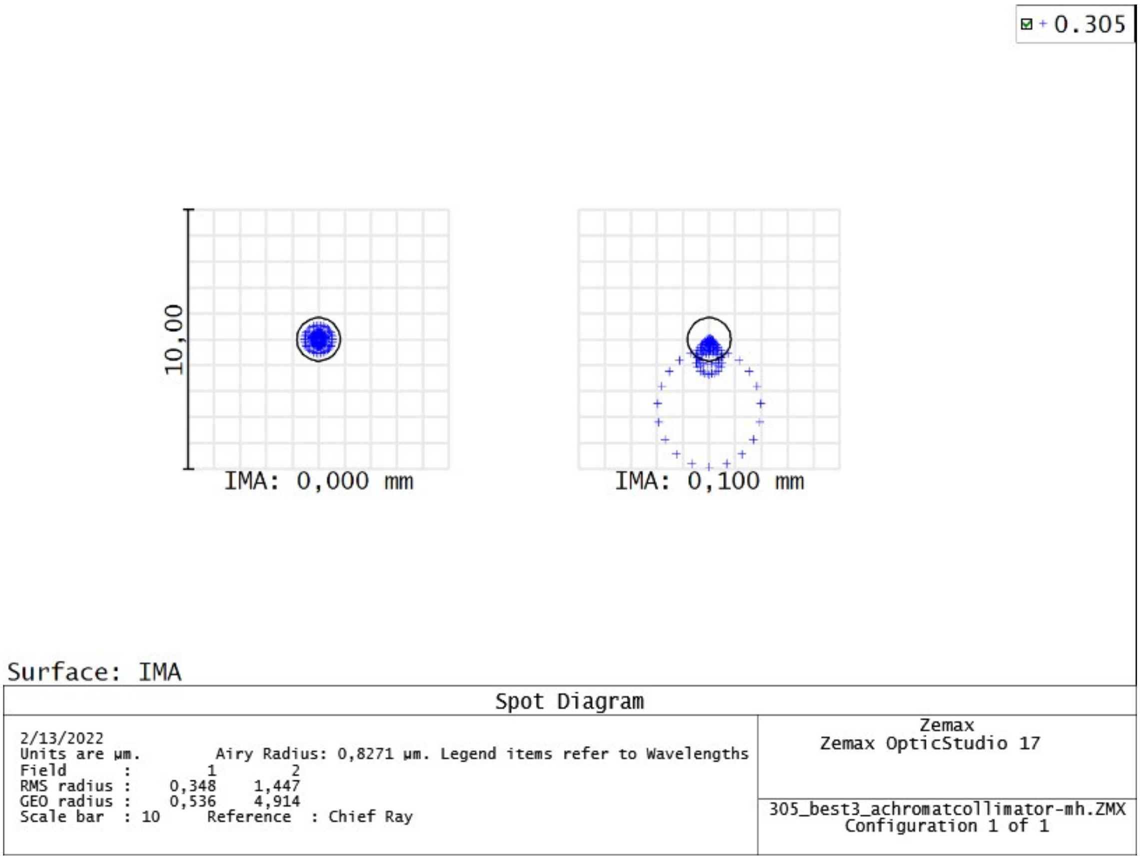

```
2/13/2022
Units are µm.        Airy Radius: 0,8271 µm. Legend items refer to Wavelengths
Field      :        1        2
RMS radius :    0,348    1,447
GEO radius :    0,536    4,914
Scale bar  : 10      Reference   : Chief Ray
```

```
305_best3_achromatcollimator-mh.ZMX
Configuration 1 of 1
```

(b) The spot diagram shows a diffraction limited Airy radius of 0.827μm. The RMS spot radius is the root-mean-square radial size and the GEO spot radius is the radius of the circle centered at the reference point which encloses all the rays. The left box shows the spot diagram of the image of an on axis point(field 1) and the right box shows the spot diagram of the image of a point 0.100mm above the optical axis(field 2). IMA stands for the IMAGE surface where the focal spot is calculated.

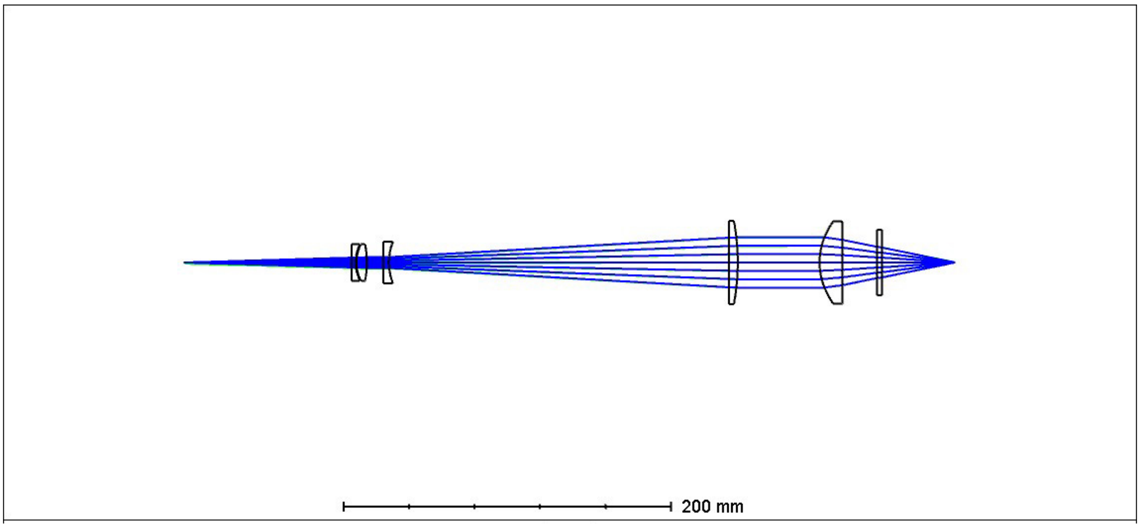

(a) Zemax OpticStudio design layout for the 243nm laser focussing.

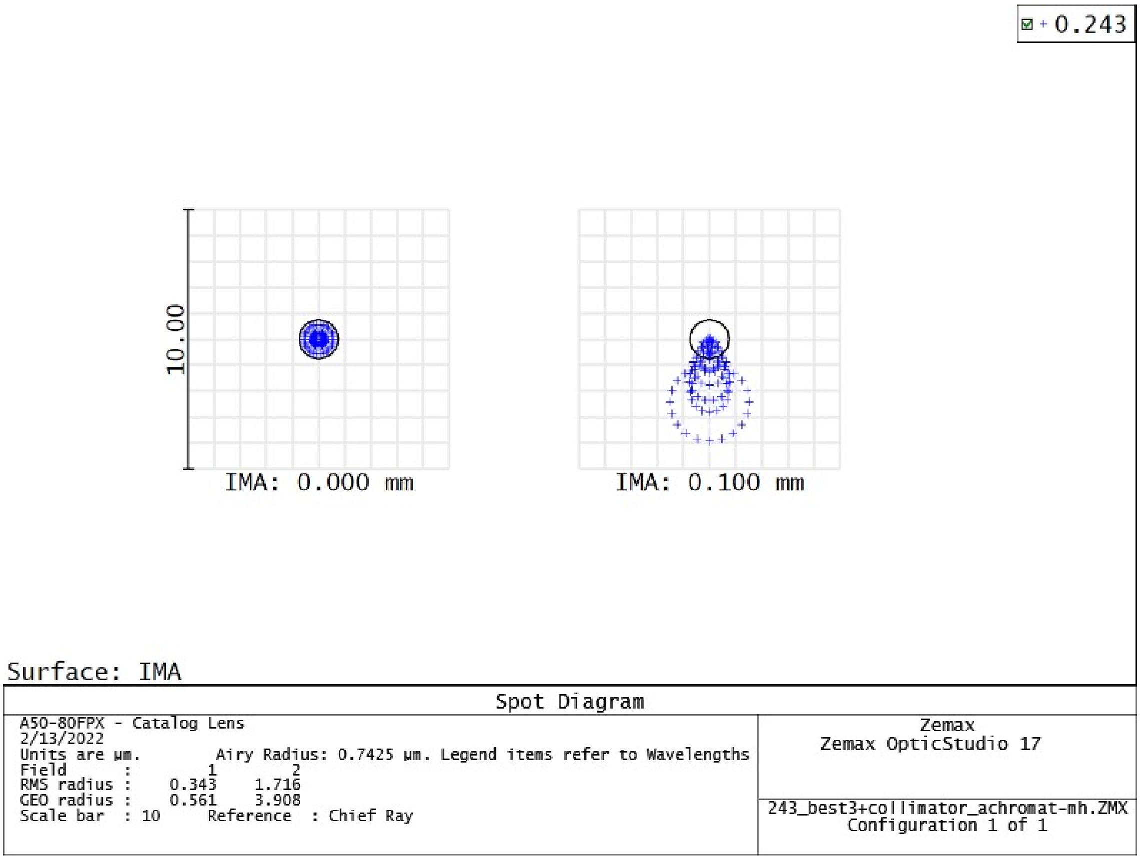

```
Spot Diagram
A50-80FPX - Catalog Lens
2/13/2022
Units are µm.        Airy Radius: 0.7425 µm. Legend items refer to Wavelengths
Field      :        1        2
RMS radius :    0.343    1.716
GEO radius :    0.561    3.908
Scale bar  : 10      Reference  : Chief Ray

Zemax
Zemax OpticStudio 17

243_best3+collimator_achromat-mh.ZMX
Configuration 1 of 1
```

(b) The spot diagram shows a diffraction limited Airy radius of $0.742\mu m$. The RMS spot radius is the root-mean-square radial size and the GEO spot radius is the radius of the circle centered at the reference point which encloses all the rays. The left box shows the spot diagram for an on axis point(field 1) and the right box shows the spot diagram for a point 0.100mm above the optical axis(field 2). IMA stands for the IMAGE surface where the focal spot is calculated.

3.2.8 Polarization gradient cooling

For experiments involving long string of ions, polarization gradient cooling(PGC) is more efficient than Doppler cooling for reaching the motional ground state. Two counter-propagating laser beams at 422nm with orthogonal polarization detuned by $\Delta = 2\pi \times 440$MHz from the cooling transition, were set up at 45° with respect to the trap axis to address all the motional modes. These are labelled as 422-t and 422-b for the top and bottom beams respectively(see figure 3.1). The experimental sequence is as follows- The Doppler cooled ions are first prepared in the $5S_{\frac{1}{2}}$ state by optical pumping. This is followed by applying the Sisyphus cooling pulses and scanning the first order sidebands to map the motional state using the 674nm laser pulse. Finally quantum state detection is performed via fluorescence detection at 422nm. Cooling to the motional ground state prevents population from $5S_{\frac{1}{2}}$ to be transfered to $4D_{\frac{5}{2}}$ while driving a red sideband (as explained previously in section 3.2.2). Reduction in the population in the $4D_{\frac{5}{2}}$ excited state indicates better cooling as can be seen from figure 3.13

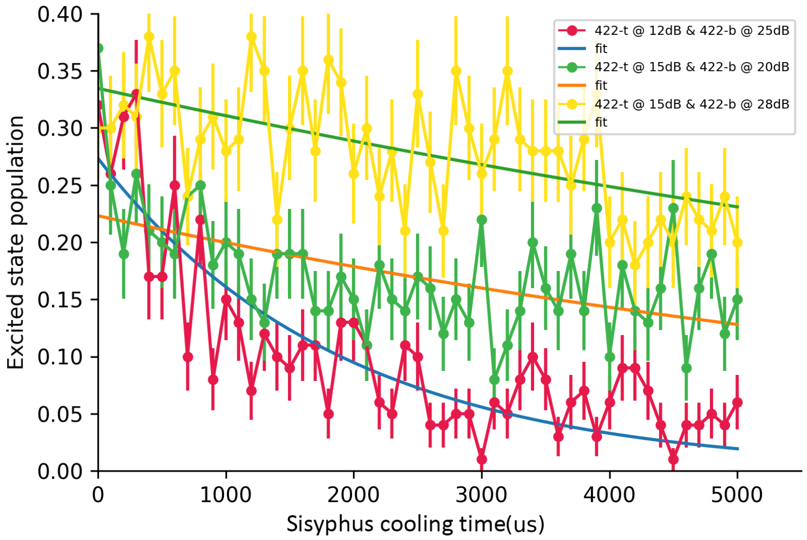

Figure 3.13: Effect of laser intensity on cooling. The three curves shows the reduction in population in the excited state when a fist order red sideband is driven. Different settings of power on the two polarization gradient beam give different cooling rate. Error bars indicate quantum projection noise (68% confidence interval).

Due to differences in fiber coupling, the power on the two PGC beams were different. Therefore optimum acousto optic modulator(AOM) settings had to be found to match the intensity sent on the two PGC beams so that the Stark effect on the ion from the two beams are similar and the momentum kick imparted in either direction is symmetric. For this, a measurement was done by driving the motional first order red sideband for different combination of AOM attenuation settings for the two beams (figure 3.13). The cooling rate was found to be highest for the setting when the AOMs corresponding to 422-t and 422-b are set to 12dB and 25dB respectively. The plot shows that at the optimal settings, there is a 40% reduction in the excited state population as compared to non optimal values and cooling works well when the sideband is driven for ≈5ms with a cooling rate of ≈550 s^{-1}.

To characterize the polarization gradient cooling, it is first demonstrated using a single ion. By driving carrier transition Rabi oscillations on $5S_{\frac{1}{2}}$ to $4D_{\frac{5}{2}}$ the effect of Sisyphus cooling could be observed as shown in figure 3.14. When Sisyphus cooling pulses are off, the strength of driving the carrier transition is reduced which is observed from the contrast of the Rabi oscillation (figure 3.14). This means that the mean phonon number is reduced when the Sisyphus cooling pulses are on, such that the coupling strength of the carrier is higher compared to the case when the Sisyphus cooling pulses are absent. This follows from the relation of the carrier

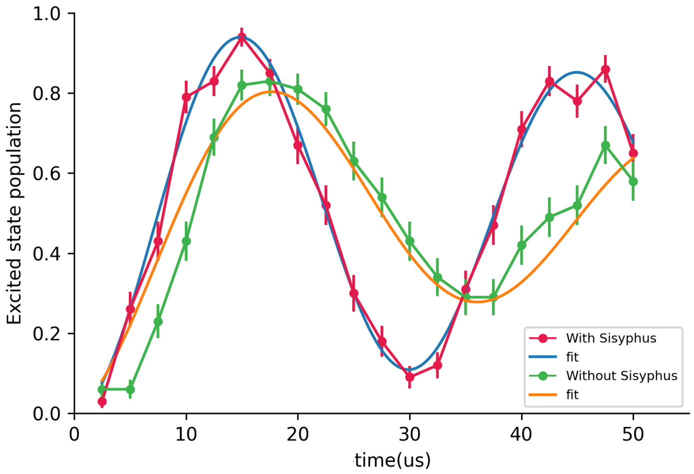

Figure 3.14: Effect of Sisyphus cooling on single ion carrier Rabi oscillation. The plot is fitted using the temperature dependent model given in section 3.2.2 by equation 3.7. Error bars indicate quantum projection noise (68% confidence interval).

coupling strength to the mean phonon number given by equation 3.2.
To demonstrate cooling of a string of ions, six ions were loaded and Doppler cooled. Figure 3.15 shows the CCD image of six ions in the trap. Using a carrier transition

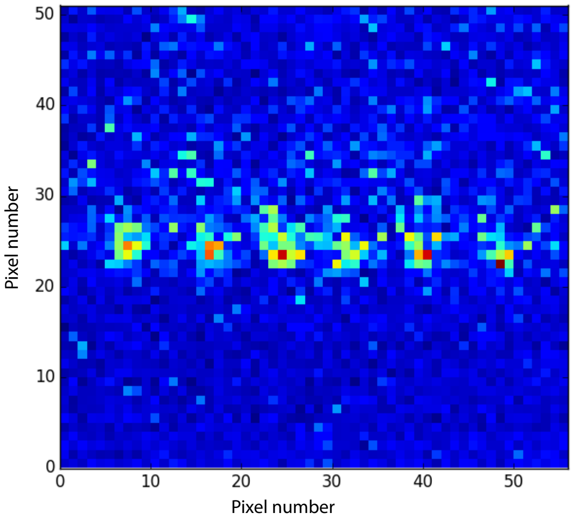

Figure 3.15: A linear chain of six Doppler cooled ions in the trap.

Rabi oscillations were driven on the 6 ions (figure 3.16). It was seen that the oscillations were driven only on three of the six ions. This is most likely because either the cooling beam or the addressing beam were not well aligned on all the six ions.

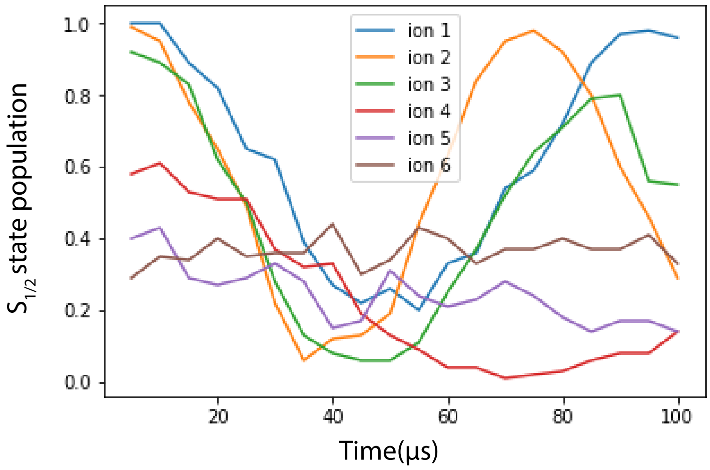

Figure 3.16: Rabi oscillation on a linear chain of six ions. The ions are numbered from left to right in figure 3.15

This will be investigated later and needs to be improved. Since all the ions were not cooled equally, a comparison of cooling single ion and string of ions couldn't be done at the time of writing.

Chapter 4

Summary and next steps

To summarize, in this report the experimental set up for trapped Rydberg ion gates is introduced. In order to cool long string of ions, optics for polarization gradient cooling has been set up and the effects of PGC has been observed. The addressing optics for UV and 674nm are identified and simulations to minimize the focal spot at the ion's position are done using Zemax OpticStudio.

To implement quantum gates in a long ion string, single ion addressing is necessary to be able to control and realize addressed manipulation of each ion individually with 674nm and UV lasers. The focusing of the UV beam increases the power delivered at the ion's position thereby improving the Rabi frequency of the Rydberg transition and hence increase the fidelity with which entanglement gates could be performed. Implementing the focusing optics from the radial direction would reduce the effect of temperature and motion of the ion on Rydberg entanglement operation.

After finalization and procurement of the required optics this will be tested and later integrated with the ion trap set up. Once this is done AOD for switching the laser position between different ions in a string will be implemented. This is required for arbitrary single qubit rotations. Entangling gate operation can be performed, by loading strings of ion with different ion number and measurements can be done on pair of ions in the string. In order to cool long string of ions, polarization gradient cooling is set up and its effect on cooling the ion string is studied. The fidelity of the gate operation will be studied and compared with increasing number of ions in the string.

Bibliography

[1] J. I. Cirac and P. Zoller, "Quantum computations with cold trapped ions," *Physical Review Letters*, vol. 74, no. 20, pp. 4091–4094, 1995.

[2] D. J. Wineland, C. Monroe, W. M. Itano, D. Leibfried, B. E. King, and D. M. Meekhof, "Experimental Issues in Coherent Quantum-State Manipulation of Trapped Atomic Ions," *Journal of Research of the National Institute of Standards and Technology*, vol. 103, no. 3, pp. 259–328, 1998.

[3] D. Leibfried, R. Blatt, C. Monroe, and D. Wineland, "Quantum dynamics of single trapped ions," vol. 75, no. 1, pp. 281–324, 2003.

[4] Pradip K. Ghosh, *Ion Traps - Pradip K. Ghosh - Oxford University Press.* Oxford University Press, 1995.

[5] K. Mølmer and A. Sørensen, "Multiparticle entanglement of hot trapped ions," *Physical Review Letters*, vol. 82, pp. 1835–1838, mar 1999.

[6] D. Kielpinski, C. Monroe, and D. J. Wineland, "Architecture for a large-scale ion-trap quantum computer," *Nature*, vol. 417, pp. 709–711, jun 2002.

[7] M. Müller, L. Liang, I. Lesanovsky, and P. Zoller, "Trapped Rydberg ions: From spin chains to fast quantum gates," *New Journal of Physics*, vol. 10, p. 093009, sep 2008.

[8] C. Zhang, *Fast and Scalable Entangling Gate in Trapped Ions via Rydberg Interaction.* PhD thesis, Stockholm University, 2020.

[9] F. G. Major, V. N. Gheorghe, and G. Werth, *Charged Particle Traps: Physics and Techniques of Charged Particle Field Confinement*, vol. 37. 2006.

[10] G. Higgins, *A Single Trapped Rydberg Ion.* Springer Theses, Cham: Springer International Publishing, 2019.

[11] G. Higgins, F. Pokorny, C. Zhang, and M. Hennrich, "Highly Polarizable Rydberg Ion in a Paul Trap," *Physical Review Letters*, vol. 123, 2019.

[12] G. Higgins, C. Zhang, F. Pokorny, H. Parke, E. Jansson, S. Salim, and M. Hennrich, "Observation of second- And higher-order electric quadrupole interactions with an atomic ion," *Physical Review Research*, vol. 3, no. 3, p. 32032, 2021.

[13] C. Zhang, F. Pokorny, W. Li, G. Higgins, A. Pöschl, I. Lesanovsky, and M. Hennrich, "Submicrosecond entangling gate between trapped ions via Rydberg interaction," *Nature*, vol. 580, pp. 345–349, apr 2020.

[14] D. J. Wineland, J. Dalibard, and C. Cohen-Tannoudji, "Sisyphus cooling of a bound atom," *Journal of the Optical Society of America B*, vol. 9, p. 32, jan 1992.

[15] J. I. Cirac, R. Blatt, A. S. Parkins, and P. Zoller, "Laser cooling of trapped ions with polarization gradients," *Physical Review A*, vol. 48, pp. 1434–1445, aug 1993.

[16] M. K. Joshi, A. Fabre, C. Maier, T. Brydges, D. Kiesenhofer, H. Hainzer, R. Blatt, and C. F. Roos, "Polarization-gradient cooling of 1D and 2D ion Coulomb crystals," *New Journal of Physics*, vol. 22, p. 103013, oct 2020.

[17] C. Foot, *Atomic Physics - C.J. Foot - Oxford University Press.* Oxford University Press, 2004.

[18] M. Brownnutt, V. Letchumanan, G. Wilpers, R. C. Thompson, P. Gill, and A. G. Sinclair, "Controlled photoionization loading of 88Sr+ for precision ion-trap experiments," *Applied Physics B: Lasers and Optics*, vol. 87, pp. 411–415, may 2007.

[19] F. Pokorny, "Experimental setup for trapping strontium Rydberg ions," tech. rep., 2014.

[20] A. Pöschl, *Laser Ablation Loading and Single Ion Addressing of Strontium in a Linear Paul Trap.* Master thesis, Technical University Munich and the Royal Institute of Technology in Stockholm, 2018.

[21] C. F. Roos, *Controlling the quantum state of trapped ions.* Phd. thesis, Leopold-Franzens-Universität Innsbruck, 2000.

[22] D. I. M. Niedermayr, *Cryogenic surface ion traps.* PhD thesis, Universität Innsbruck, 2015.

[23] D. J. Berkeland, J. D. Miller, J. C. Bergquist, W. M. Itano, and D. J. Wineland, "Minimization of ion micromotion in a Paul trap," *Journal of Applied Physics*, vol. 83, pp. 5025–5033, may 1998.

[24] J. Keller, H. L. Partner, T. Burgermeister, and T. E. Mehlstäubler, "Precise determination of micromotion for trapped-ion optical clocks," *Journal of Applied Physics*, vol. 118, may 2015.

[25] G. Higgins, S. Salim, C. Zhang, H. Parke, F. Pokorny, and M. Hennrich, "Micromotion minimization using Ramsey interferometry," *New Journal of Physics*, vol. 23, p. 123028, dec 2021.

[26] G. Higgins, F. Pokorny, C. Zhang, Q. Bodart, and M. Hennrich, "Coherent Control of a Single Trapped Rydberg Ion," *Physical Review Letters*, vol. 119, p. 220501, nov 2017.